Supplemental Material

Supplemental Material for "Arctic Sea Ice Growth in Response to Synoptic- and Large-scale Atmospheric Forcing from CMIP5 Models"

1. CMIP5 model selection

In this study, we apply the combined metrics ranking method developed by Cai et al. (2018), to select relatively more successful modeling for further analysis. The ranking prioritizes how successful CMIP5 models reproduce the Arctic Dipole (AD) pattern in winter (December-January-February; DJF). For every single model, the dipole-shaped pattern of the AD is sought in the second to the fifth mode of the EOF calculated based on the DJF Sea-Level-Pressure (SLP) pattern in the period of 1950-2005. Winter AD in the NCEP/NCAR reanalysis data serves as the reference, which is calculated using the same method in the same base period (1950-2005). The calculated winter AD patterns (if any) of the thirty CMIP5 models are in Fig. S1.

The combined metrics ranking method combines the Pattern Correlation Coefficients (PCCs) with the explained variances of the corresponding EOF mode, aiming to give an overall quantitative evaluation of how successful each model can produce winter AD. Before calculating PCC, both the patterns of the CMIP5 model and the reference are regridded to the ACCESS1.0's grid that is close to the median resolution among all 30 models. The PCC is calculated using the following equation

$$PCC = \frac{\sum_{i=1}^{N} F_i \cdot R_i}{\left[\sum_{i=1}^{N} (F_i)^2 \cdot \sum_{i=1}^{N} (R_i)^2\right]^{1/2}} \quad (1)$$

where F_i and R_i represent N EOF grid point values from respectively the CMIP5 model and the reference dataset (regridded).

A score for the combined metrics ranking is calculated using the following equation:

$$S = \sqrt{\sum_{i=1}^{m} (\Delta P_i)^2} \quad (2)$$

in which ΔP_i is the difference from the i^{th} model parameter (PCCs and explained variances of the winter AD) to the corresponding reference after a feature scaling. The feature scaling normalizes the vector components by rescaling the sample range to one using the formula as follows.

$$x' = \frac{x}{\max(x) - \min(x)} \quad (3)$$

where $\max(x)$ and $\min(x)$ are, respectively, the largest and the smallest values in the sample. The final ranking of the 30 CMIP5 models in reproducing the winter AD is listed in Table S1.

Rank	model	EOF mode	Explained Variance	PCC	RMSE	Combined Metrics Score
	NCEP/NCAR	**2nd**	**12.5**	**1**	**0**	**0**
1	MPI-ESM-LR	2nd	16.4	0.90	0.23	0.182
2	CSIRO-Mk3-6-0	2nd	16.7	0.88	0.28	0.257
3	MIROC5	2nd	18	0.88	0.27	0.269
4	HadGEM2-CC	3rd	14.8	0.87	0.28	0.283
5	ACCESS1-3	2nd	18.6	0.87	0.27	0.295
6	HadGEM2-AO	3rd	12.2	0.93	0.20	0.349
7	MRI-CGCM3	2nd	19.9	0.83	0.30	0.401
8	GISS-E2-H-CC	2nd	11.2	0.95	0.15	0.408
9	GISS-E2-R	2nd	17.6	0.79	0.35	0.415
10	CCSM4 (CAM4)	2nd	15.2	0.79	0.35	0.425
11	ACCESS1-0	2nd	19.3	0.80	0.34	0.434
12	CNRM-CM5	2nd	20.7	0.83	0.31	0.440
13	CMCC-CM	2nd	15.1	0.76	0.38	0.486
14	CESM1 (CAM5)	3rd	11.4	0.83	0.31	0.501
15	HadGEM2-ES	2nd	20.4	0.79	0.37	0.502
16	GFDL-ESM2M	2nd	16.8	0.68	0.44	0.621
17	GFDL-ESM2G	3rd	10.1	0.76	0.36	0.670
18	GISS-E2-R-CC	3rd	7.2	0.98	0.10	0.697
19	GISS-E2-H	2nd	12.5	0.67	0.43	0.711
20	IPSL-CM5B-LR	2nd	10.7	0.68	0.44	0.769
21	IPSL-CM5A-LR	3rd	8.6	0.75	0.39	0.772
22	MIROC-ESM	3rd	10.5	0.68	0.44	0.777
23	MRI-ESM1	3rd	9.7	0.66	0.44	0.841
24	CanESM2	2nd	11.8	0.61	0.50	0.844
25	IPSL-CM5A-MR	3rd	7.5	0.70	0.43	0.887
26	CMCC-CMS	3rd	11.3	0.58	0.52	0.911
27	MIROC-ESM-CHEM	2nd	14.1	0.49	0.56	1.017
28	inmcm4	N/A	N/A	N/A	N/A	N/A
28	NorESM1-M	N/A	N/A	N/A	N/A	N/A
28	NorESM1-ME	N/A	N/A	N/A	N/A	N/A

Table S1. Ranking of the CMIP5 models after combined metrics ranking.

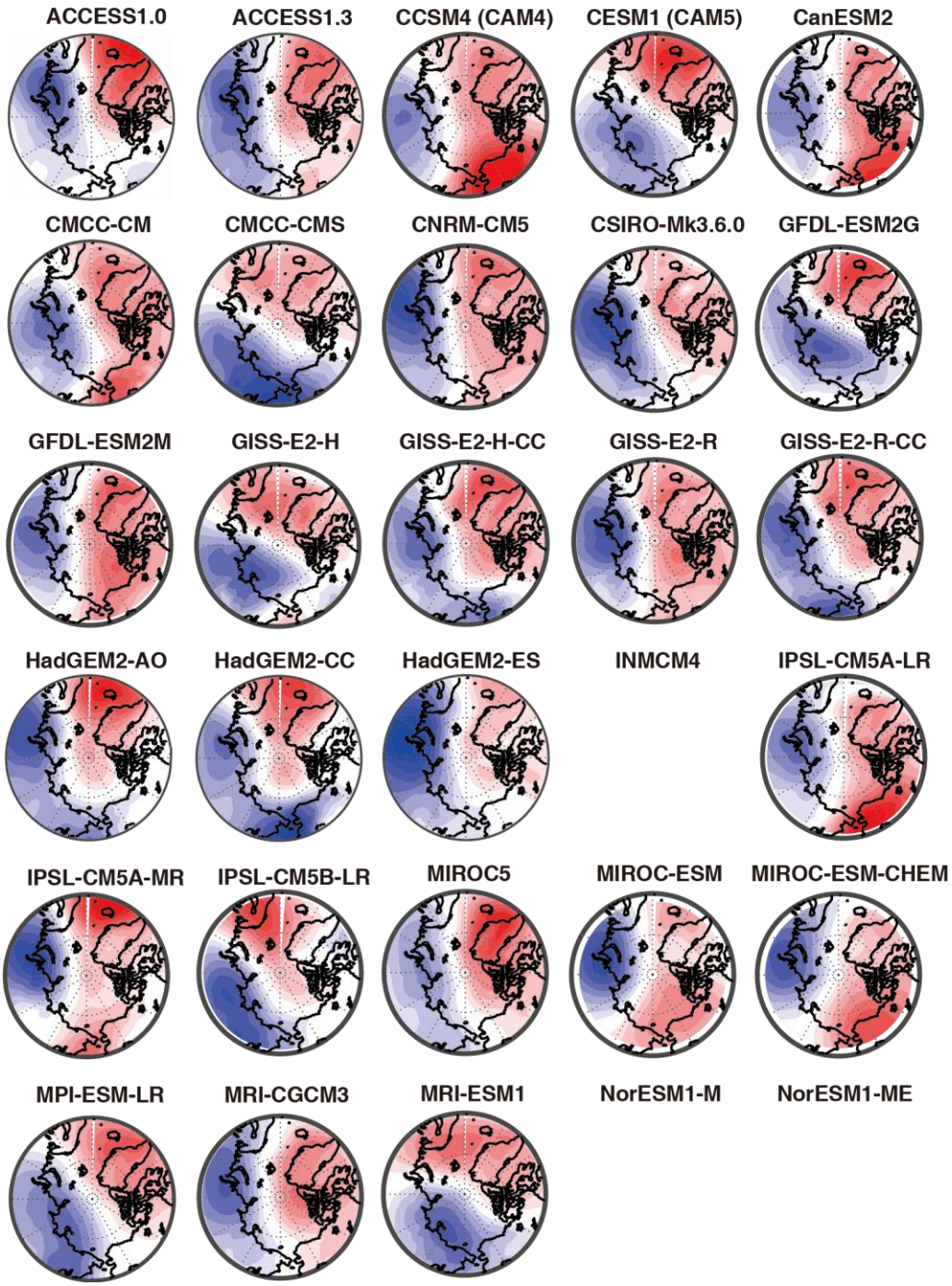

Fig. S1. Winter AD patterns (if any) of the thirty CMIP5 models.

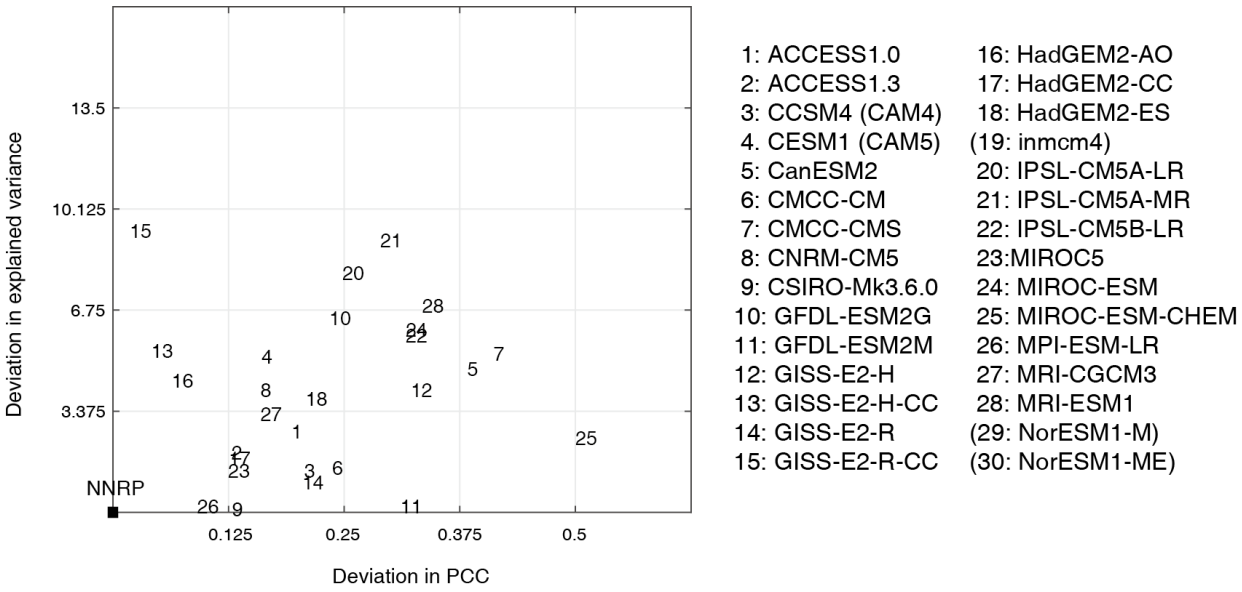

Fig. S2. The normalized deviations of PCC and explained variance of 30 CMIP5 models in reproducing the AD in winter, compared to those in NCEP/NCAR reanalysis data.

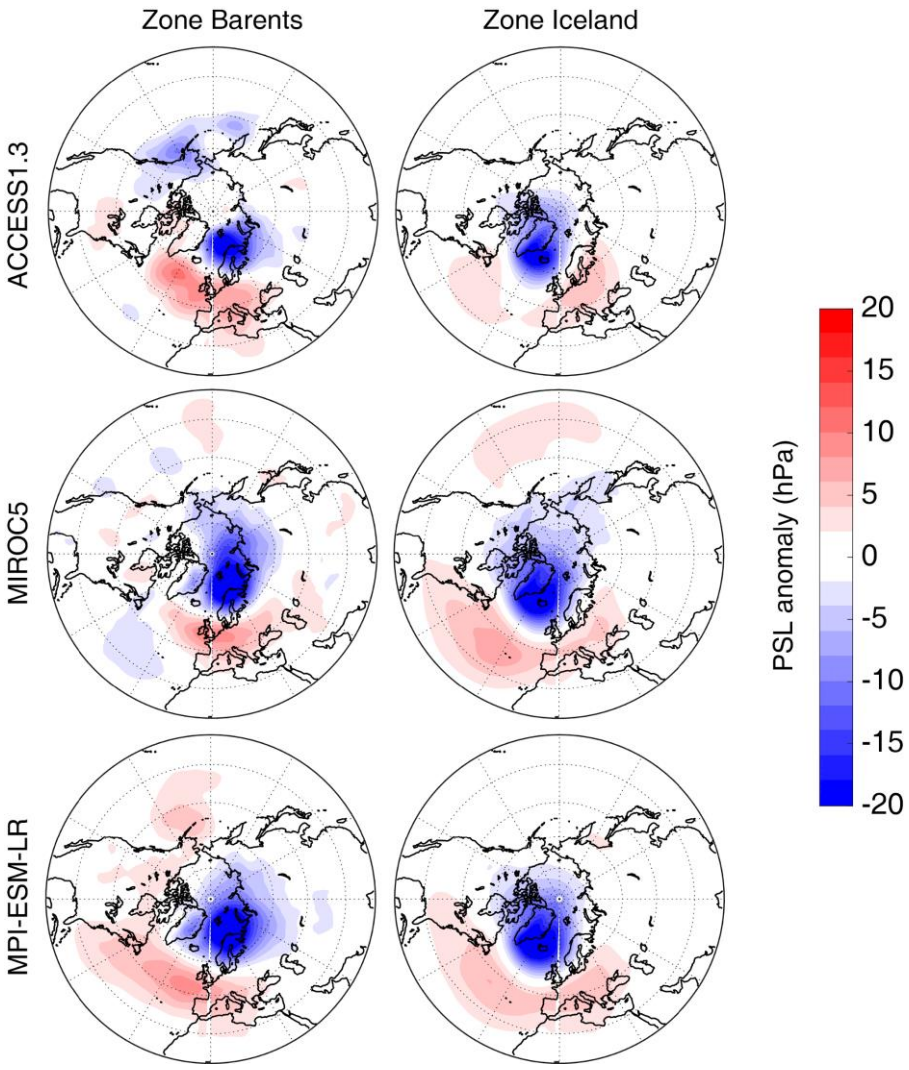

Fig. S3. Composite of model-produced PSL anomaly for cyclones in both zones in the historical period (1950-2005).

2. The response of the surface energy budget

In this section, we analyze the response of sensible heat flux and the surface energy budget. Fig. S4 and S5 show the anomalies of sensible heat flux in response to strong cyclones (in both zones) and large scale circulation patterns (negative AD and positive AO). For all circumstances, the anomaly cannot reach the polar cap, meaning the sensible heat flux can barely make impacts to the surface energy budget over the polar cap. Fig. S6 and S7 show the response of the residual of surface energy budget to strong cyclones and large-scale circulation patterns, in which the positive anomaly means there is more energy going down into the surface (the sea surface or sea ice surface in this case). The spatial patterns of the anomaly of the residual of surface energy budget are very similar to those of the downwelling longwave radiation flux (DLW), so is the magnitude of anomalies for the central Arctic region. It verifies that the increase of downwelling longwave radiation flux dominates the change in surface energy budget for the central Arctic, which serves as the thermodynamic forcing influencing the thermodynamic sea ice growth rate (SGR). Over the sub-Arctic regions, the sensible heat flux change also contributes to the change in the surface energy budget, making the anomalies of the residual of the surface energy budget higher in magnitude than those of the DLW. In the RCP8.5 period, the spatial patterns of the residual of surface energy budget keep being similar to that of the DLW in response to strong cyclones and large-scale circulation patterns. The magnitudes of the residual of surface energy budget also similar between the historical period and the RCP8.5 period for the Arctic. It verifies that the thermodynamic forcing from the atmosphere does not cause the dampened sensitivity of SGR in the projected period.

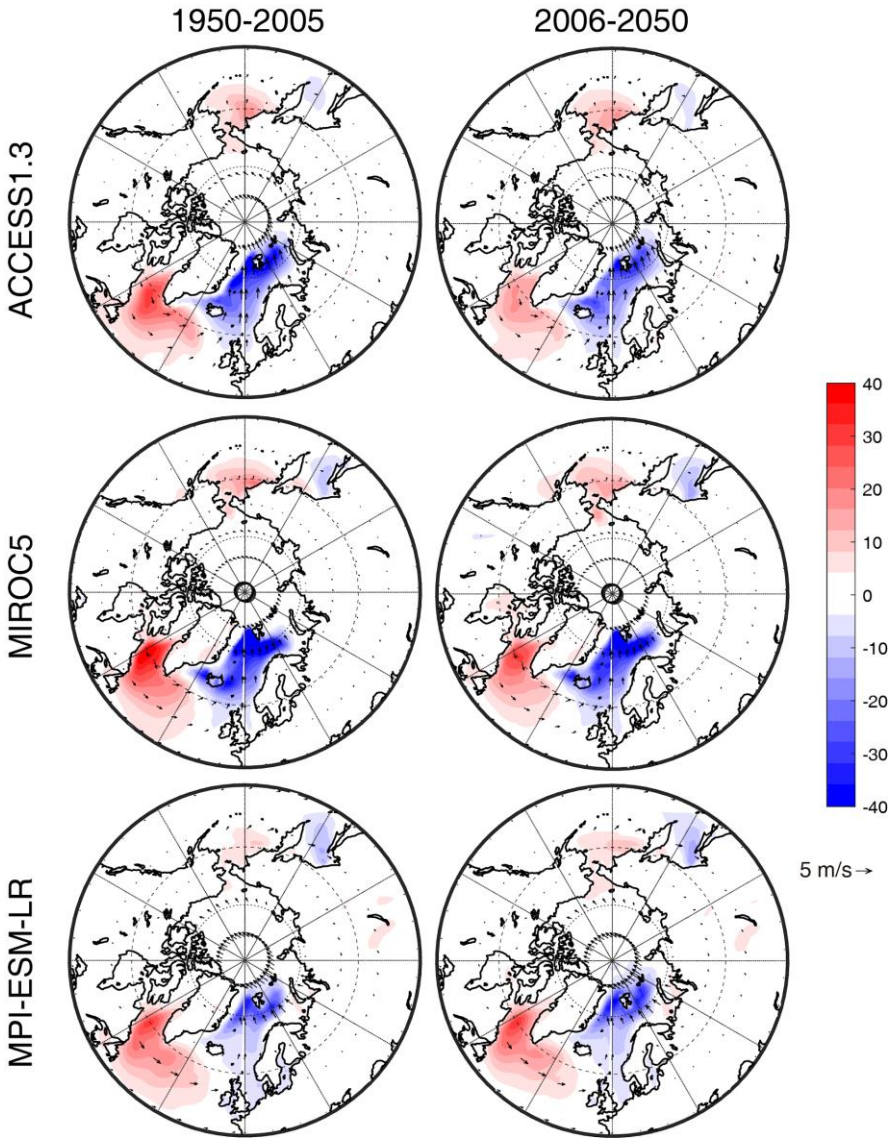

Fig. S4. The map of daily upward sensible heat flux (shaded) and wind (vector) anomalies regressed onto the daily negative AD index in the historical and RCP8.5 periods.

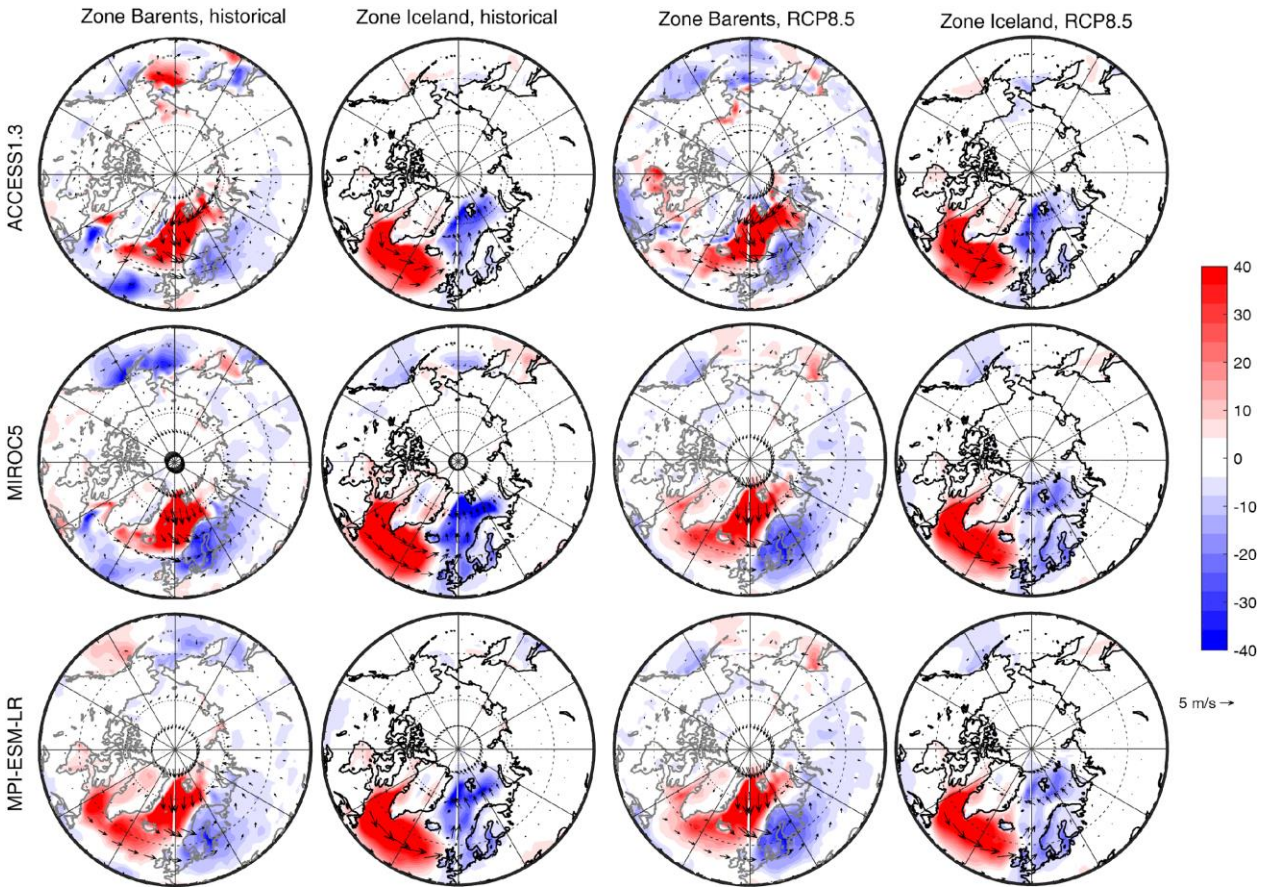

Fig. S5. Anomalies of daily upward sensible heat flux (shaded) and wind (vector) in response to the strong cyclones in Zone Barents and Zone Iceland in the four chosen models in the historical (left panel) and RCP8.5 (right panel) periods.

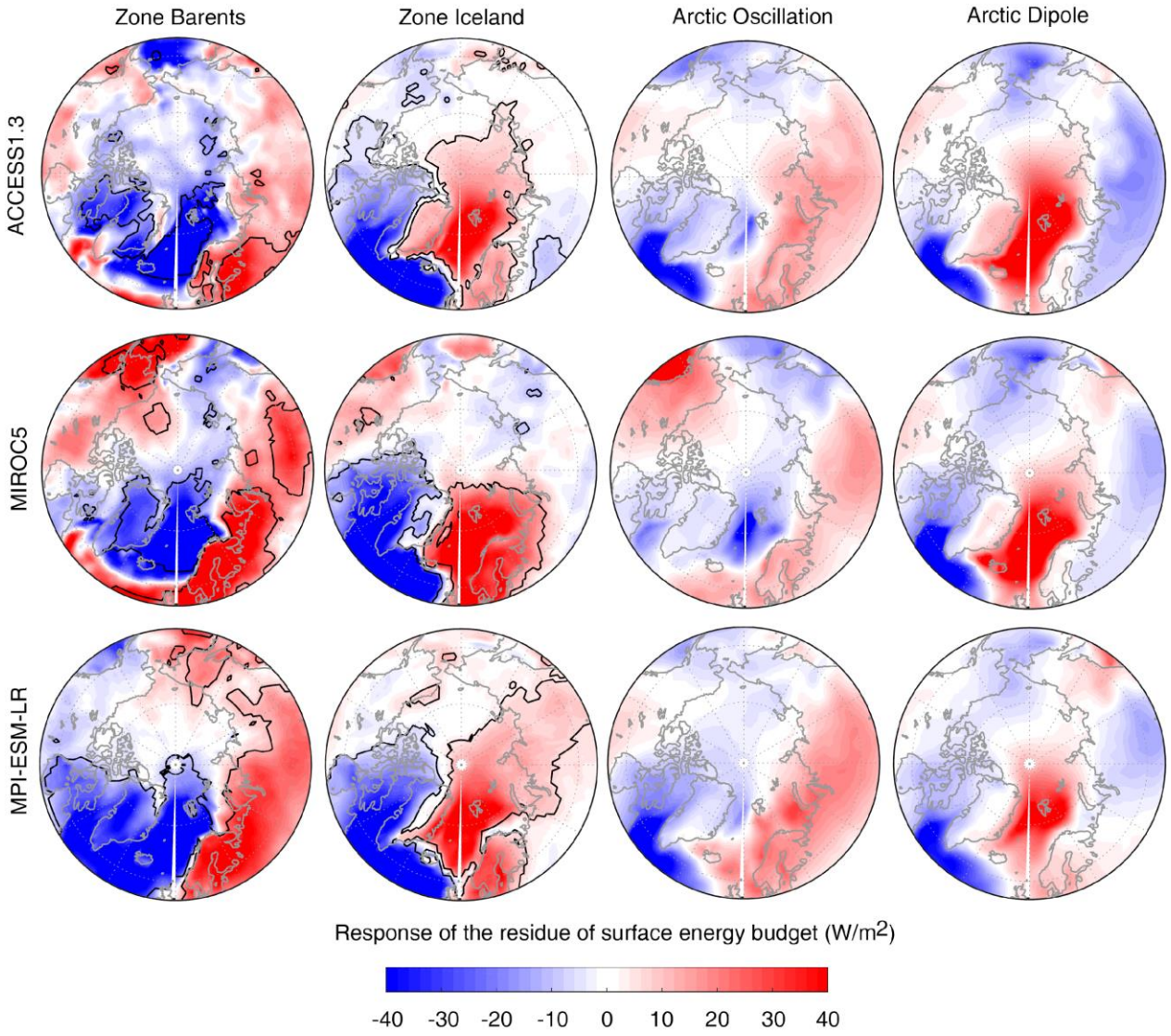

Fig. S6. Anomalies of the residual of the surface energy budget in response to strong cyclones in Zone Barents and Zone Iceland (left panel), and regressed on the positive AO and negative AD (right panel) in the historical period (1950-2005). The positive anomaly of the residual of surface energy budget means there is more energy going down under the surface (in this case the sea ice surface). The spatial distributions of the anomalies are very similar to that of DLW anomalies, showing the dominant effect of DLW as the thermodynamic forcing from the atmosphere.

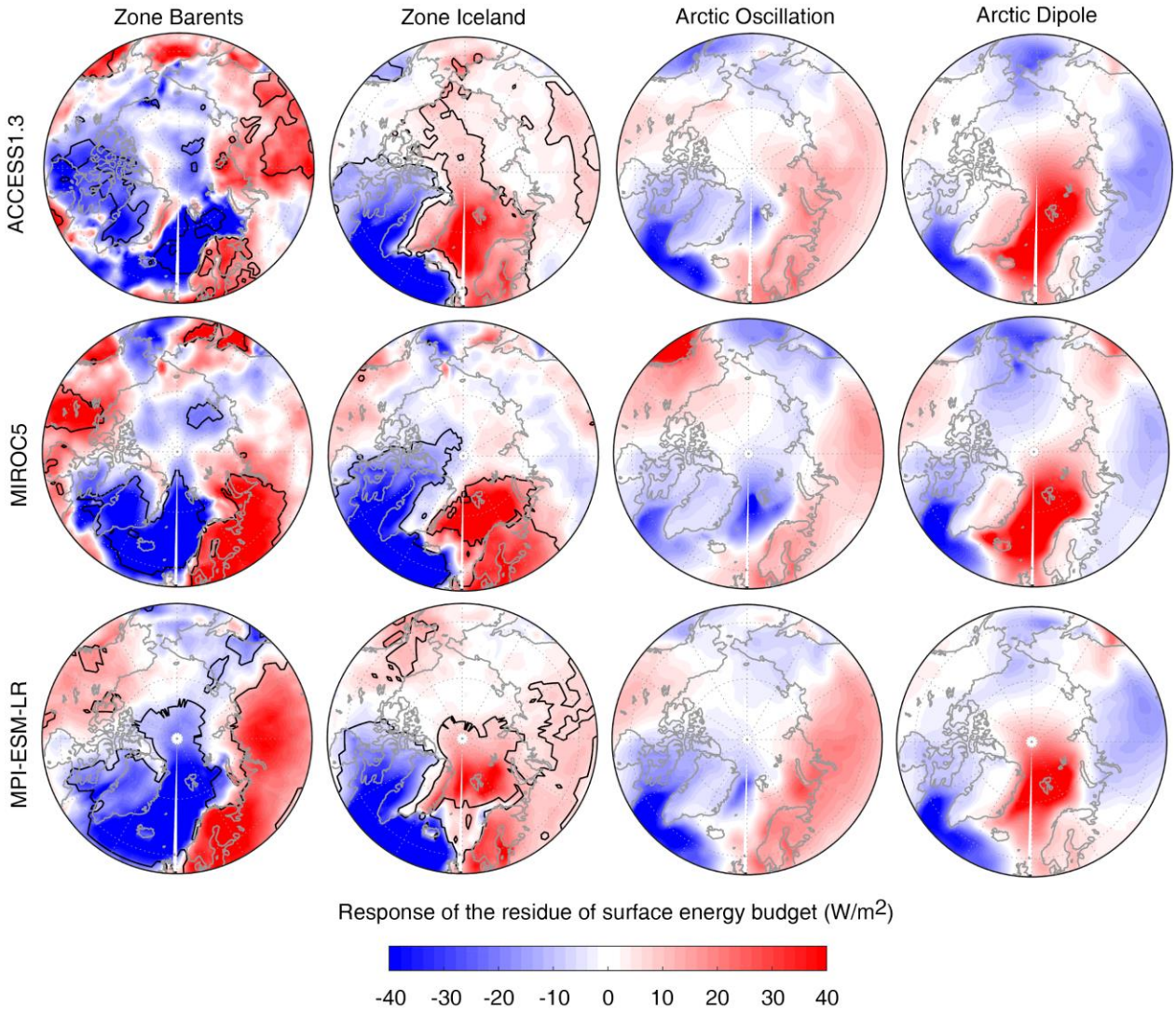

Fig. S7. As for Fig. S6, but in the RCP8.5 period (2006-2050).

3. The response of downwelling longwave radiation and sea ice growth with a lag time

In the main text, we address the response of the Sea ice Growth Rate (SGR) on a daily scale. Below is a complementary analysis being extended into an intra-seasonal timescale. Model output from GFDL-CM3 has suggested that the increased downwelling longwave radiation flux can persist even after the anomalous wind have dissipated during the whole arctic moisture intrusion event, thus continuing to serve as the thermodynamic forcing to inhibit SGR for up to more than 2 weeks (Park et al., 2015). Here we explore if such a feature exists in other CMIP5 models.

We analyze the response in all three models with lag time in terms of days with strong cyclones in Zone Iceland, as well as with strong negative AD (daily AD index < -1) in the historical period. In this case, we integrate the sea ice growth rate change from 8 days before the selected day to quantify the response during the whole life cycle. The dynamic SGR change is integrated using the formula below, following Park et al. (2015).

$$\Delta h_j = -\sum_{i=-8}^{j} \left[\frac{\partial(uh)}{\partial x} + \frac{\partial(vh)}{\partial y}\right]_i' \delta t_i$$

the prime (') denotes the deviation from the daily climatology calculated from a 21-year moving average manner mentioned in the methodology.

For both events (days) with a strong cyclonic circulation and strong negative AD circulation, the increased DLW can persist after the anomalous wind disappears (Fig S8). Although the magnitude of DLW anomaly decreases after +0 days, the DLW anomaly can spread to a wider range. At +8 days, there is hardly any wind anomaly, while there is still around 10 W/m^2 DLW anomaly over the central Arctic. In terms of sea ice responses, the accumulated thermodynamic SGR change keeps being substantially stronger than the dynamic SGR change in all three examined time points (+0, +4, +8 days) after the events. In the day -4, the dynamic SGR change can exceed the thermodynamic SGR change in limited regions. In comparison between the synoptic-scale and large-scale atmospheric forcing, the strong negative AD can lead to greater thermodynamic SGR inhibition than the strong cyclones can, which is consistent with the comparison in SGR responses in the main text.

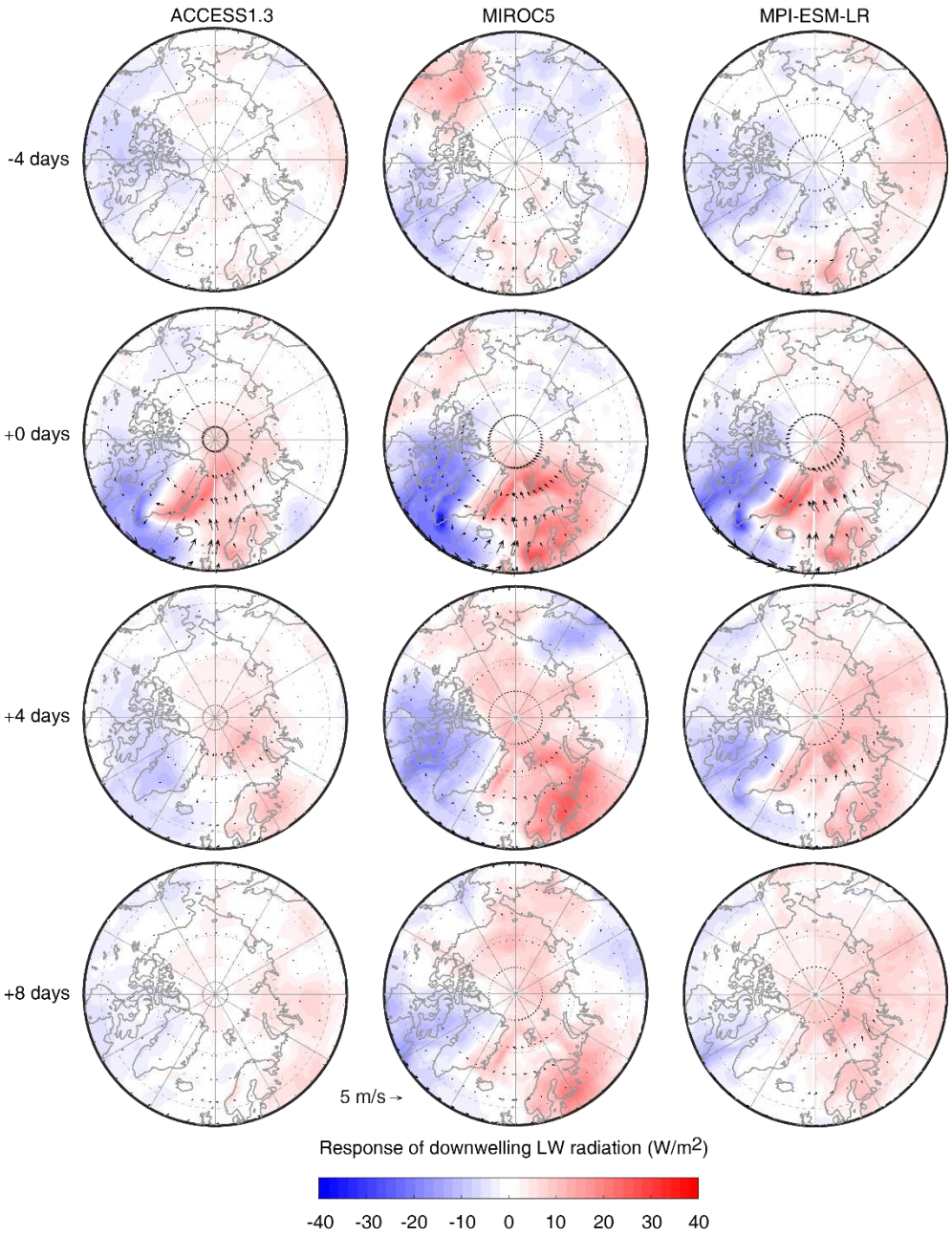

Fig S8. Anomalous DLW in response to strong cyclone in Zone Iceland in the historical period (1950-2005) with the lag time of -4, 0, +4, and +8 days.

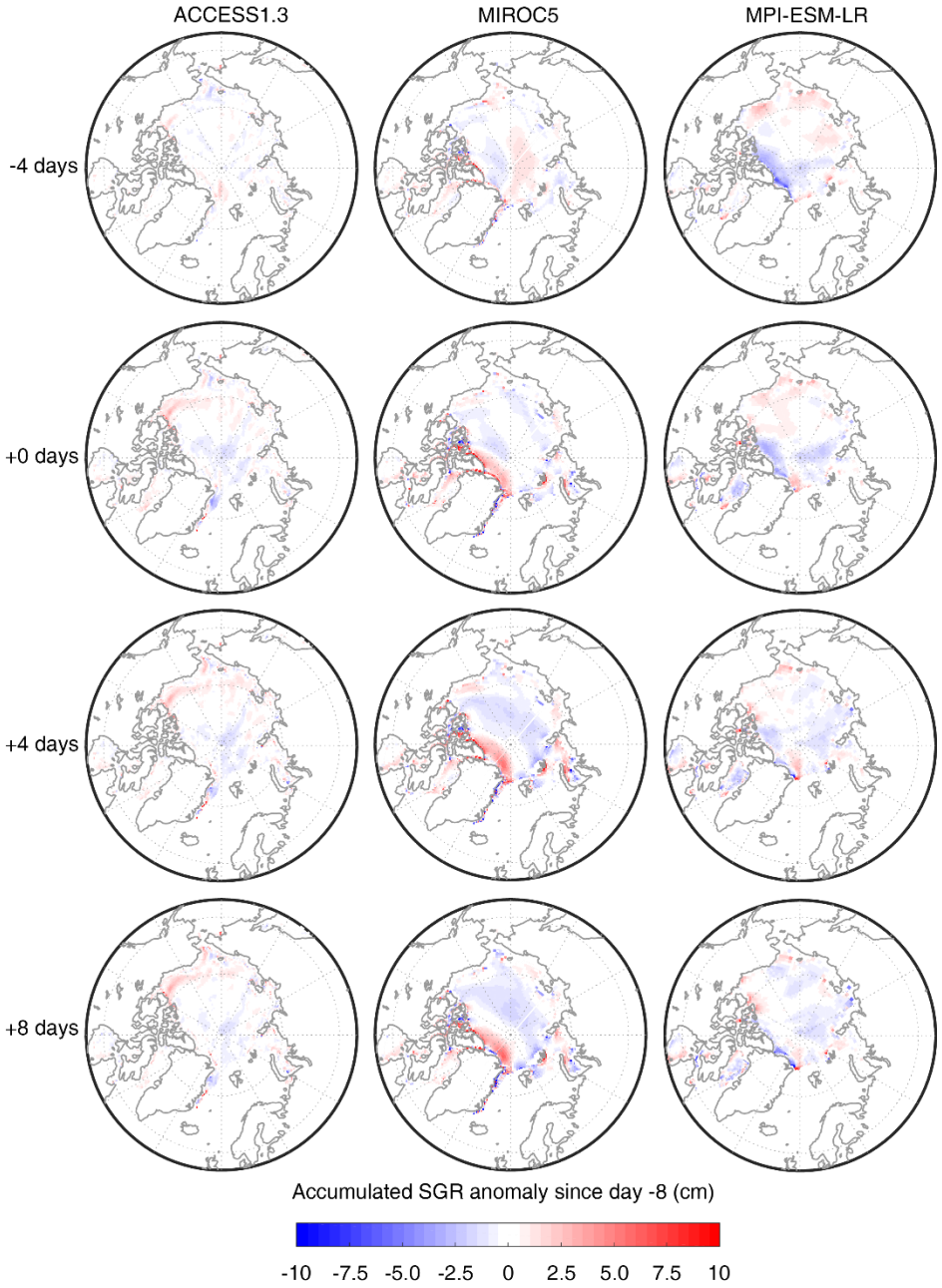

Fig S9. The accumulated SGR anomaly (cm) since -8 days due to the dynamic forcing in response to strong cyclone in Zone Iceland in the historical period (1950-2005) with the lag time of -4, 0, +4, and +8 days.

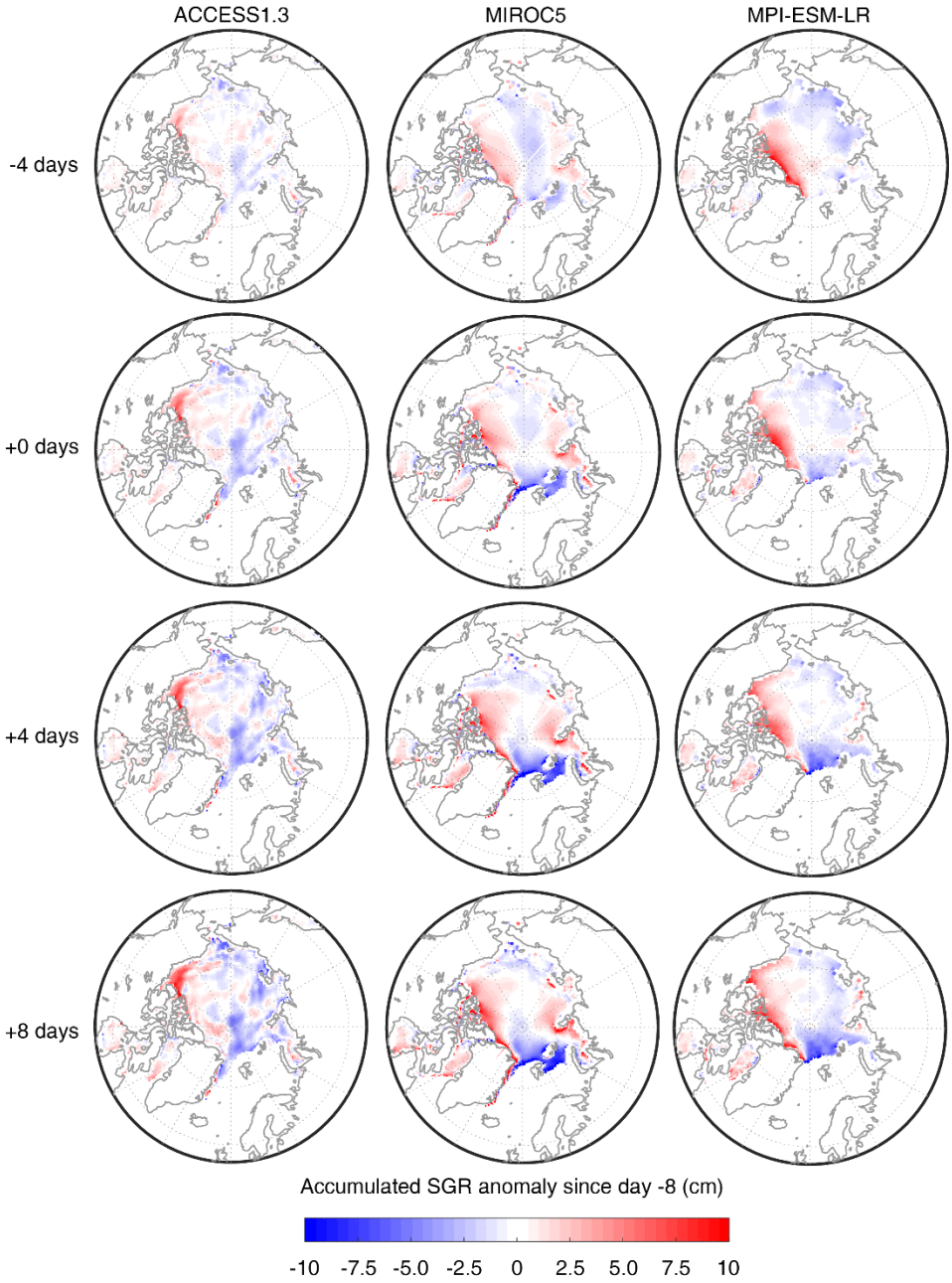

Fig S10. The accumulated SGR anomaly (cm) since -8 days due to the thermodynamic forcing in response to strong cyclones in Zone Iceland in the historical period (1950-2005) with the lag time of -4, 0, +4, and +8 days.

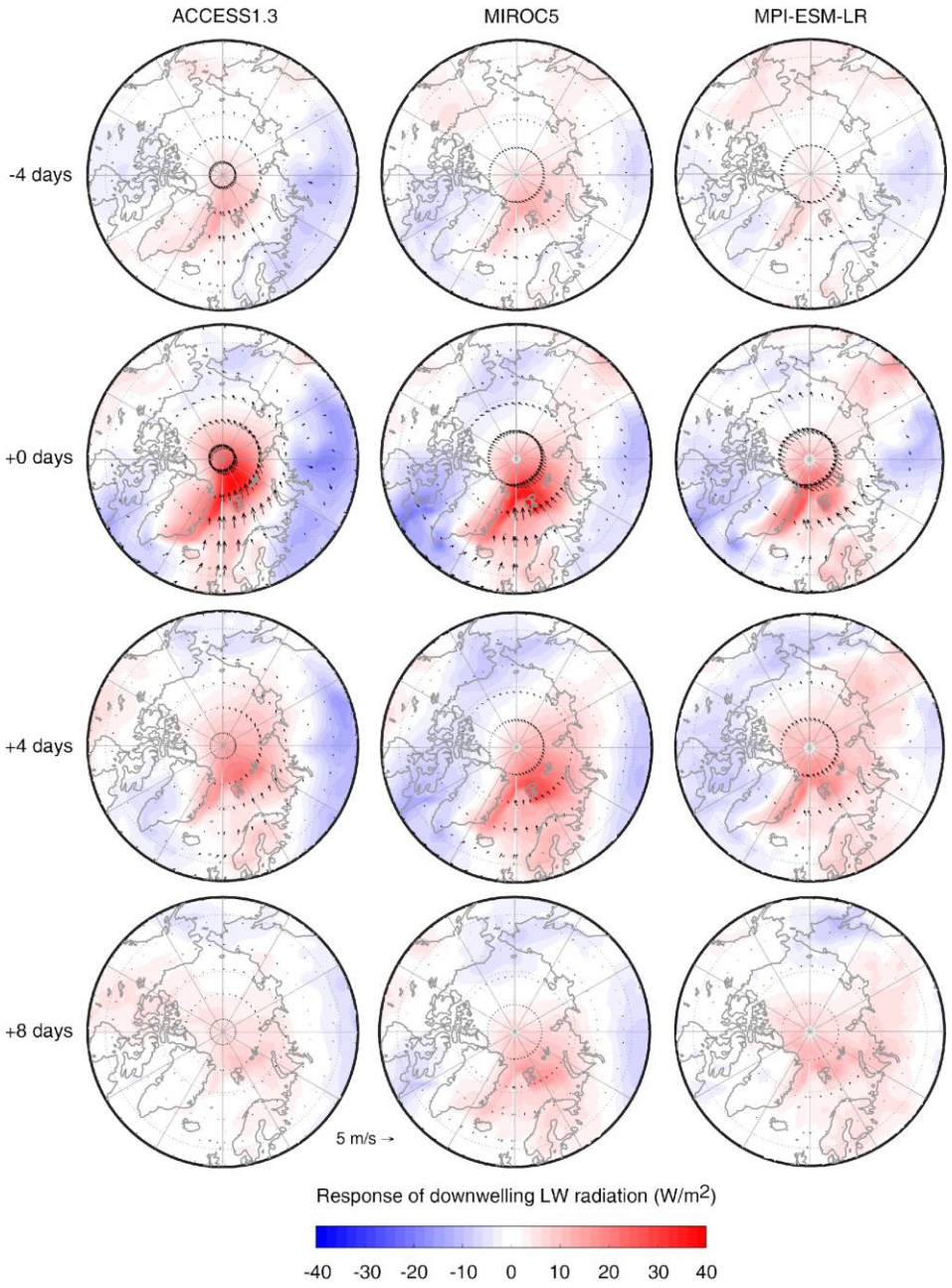

Fig S11. Anomalous DLW in response to strong negative AD (the daily AD index < -1) in the historical period (1950-2005) with the lag time of -4, 0, +4, and +8 days.

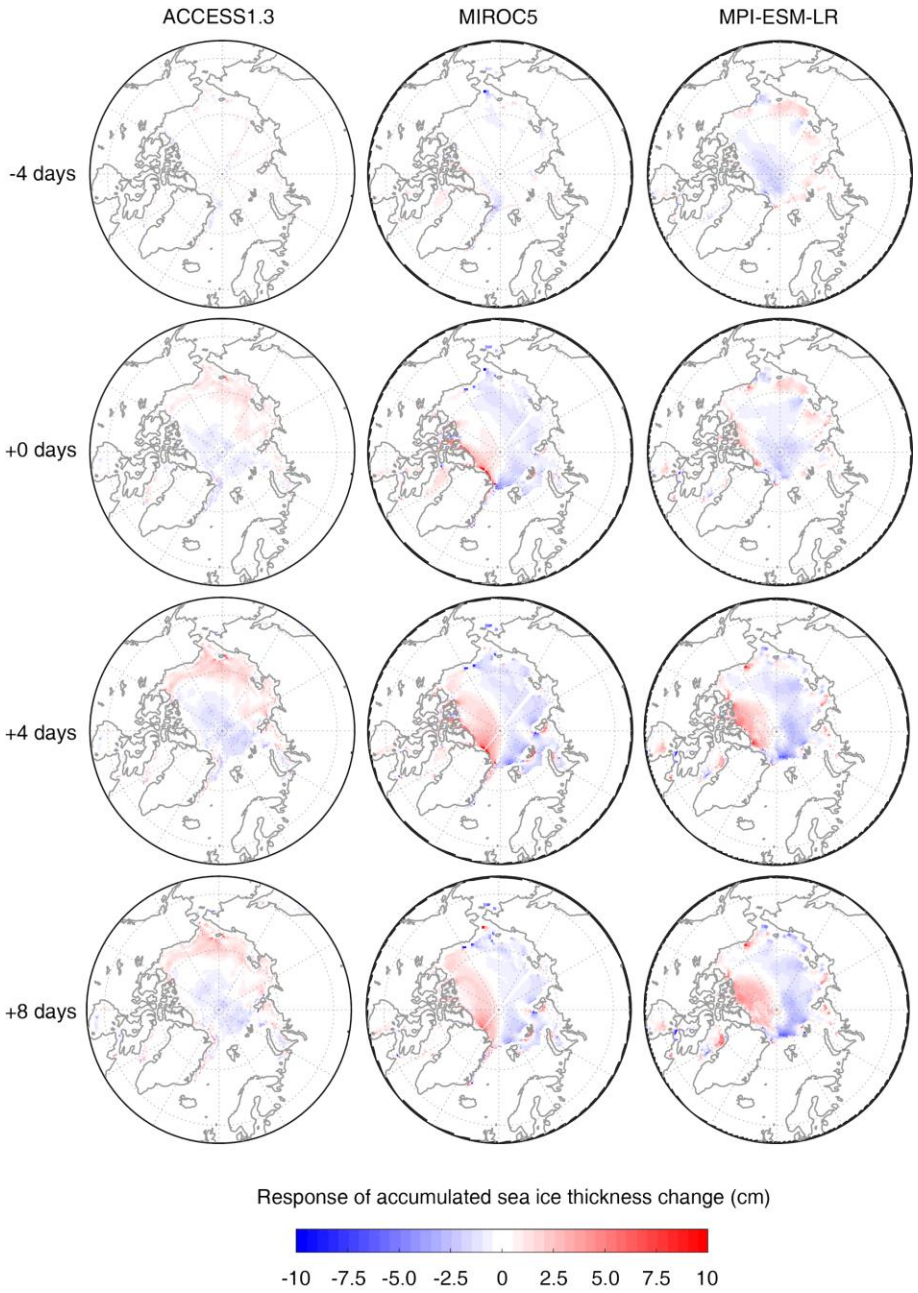

Fig S12. The accumulated SGR anomaly (cm) since -8 days due to the dynamic forcing in response to strong negative AD (the daily AD index < -1) in the historical period (1950-2005) with the lag time of -4, 0, +4, and +8 days.

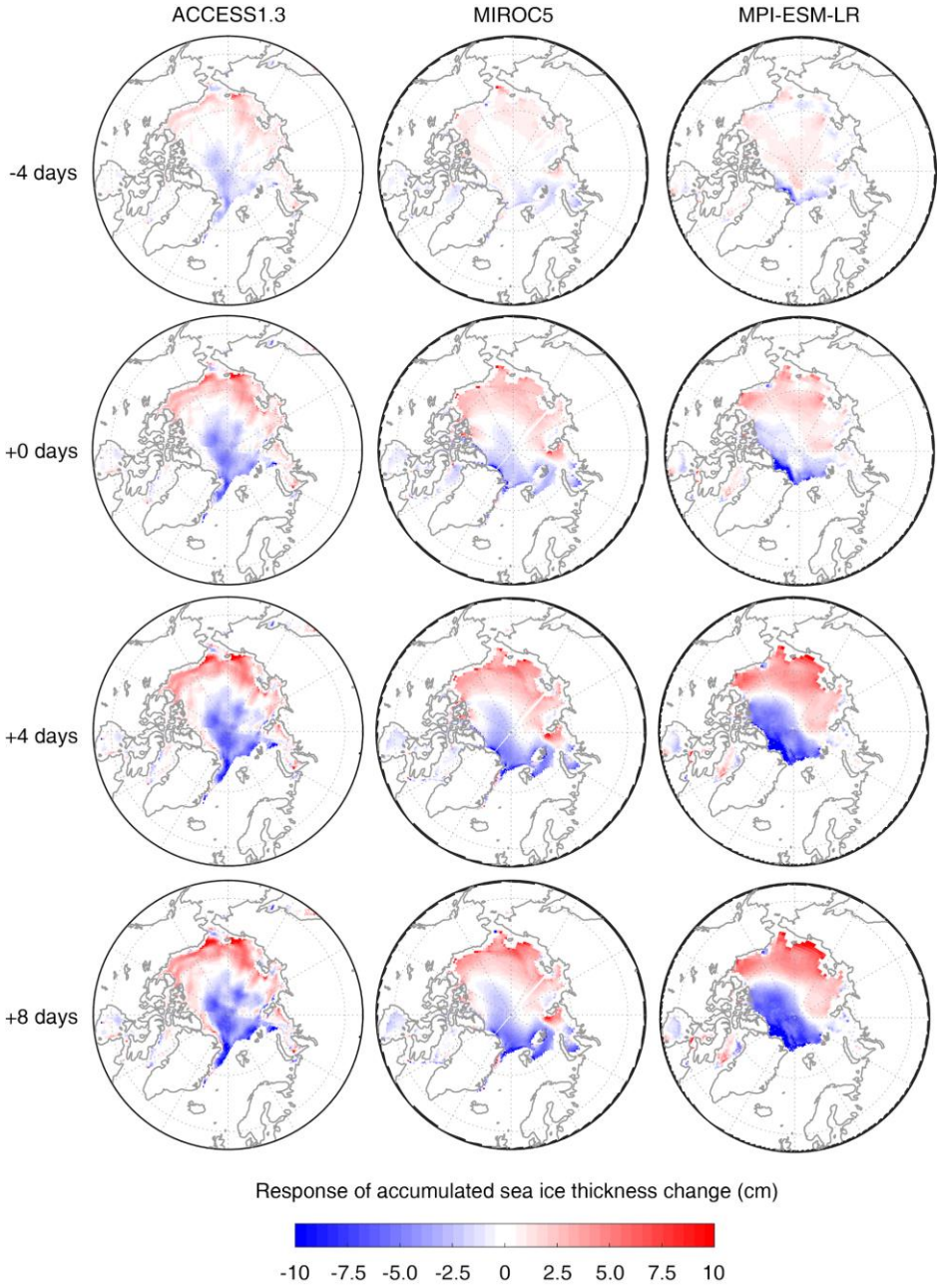

Fig S13. The accumulated SGR anomaly (cm) since -8 days due to the thermodynamic forcing in response to strong negative AD (the daily AD index < -1) in the historical period (1950-2005) with the lag time of -4, 0, +4, and +8 days.

4. Discussion on the source of inconsistencies between DLW and thermodynamic SGR

In the above section, we verify that for the central Arctic, the changes in the surface energy budget can be mostly explained by the change of DLW, while the spatial patterns of DLW and thermodynamic SGR show some inconsistency for some regions (Fig. 3, 5, 7, and 8 in the main text). In this section, we argue that such inconsistency is due to the open water ice formation, favoring by the parameterized sea ice ridging processes in the sea ice model. The open water ice formation is more efficient than the thermodynamic growth of existing ice as it forms from a different numerical implementation. Taking CICE4 as an example, the calculation of new ice formation only involves the freezing/melting potential, which is related to ocean temperature. As long as the ocean temperature is below freezing, new ice will always grow at least to a specified minimum thickness, making a fairly high SGR for the open water area of a grid (Hunke et al., 2010).

New ice formation is particularly active for the open water area in the central Arctic because of the cold temperature. In sea ice models, either sea ice divergence or sea ice ridging can change the open water area, therefore favoring or inhibiting the open water ice formation (in the next modeling time step). Here the sea ice ridging refers to any kind of mechanical redistribution of ice thickness field that leads to change in sea ice concentration while keeping sea ice volume unchanged. Because sea ice ridging does not change sea ice volume, it cannot change the average sea ice thickness. However, the opening/closing of leads because of sea ice ridging can favor/inhibit new ice formation, therefore changing the average ice thickness on the next modeling time step.

We analyze the sea ice concentration and its response to strong cyclones and large-scale circulation patterns. Fig. S14 shows the composite spatial patterns of sea ice concentration one day before the strong cyclones. Along the Arctic coast of Alaska and Siberia (the Chukchi, Beaufort, Eastern Siberia, and Laptev Seas) where the inconsistency is noticeable, the sea ice concentration when there just before strong cyclones are high (>98%) for all three models. In this way, the area change of sea ice leads from sea ice divergence is very limited. On the other hand, the three sea ice models in this study allow a maximum of 15% area of a grid to be involved in sea ice ridging, which can potentially open a substantially larger water area compared to sea ice divergence can. We therefore suggest that in our study area, the favored/inhibited open water ice formation is mostly a consequence of sea ice ridging rather than sea ice divergence.

Rather than the central Arctic, both sea ice divergence and sea ice ridging could be active along the ice edge where the sea ice typically thinner and with a lower concentration. Other than the inhibition of thermodynamic sea ice growth, atmospheric forcing can also lead to a decrease in sea ice concentration and also a more distinctive inconsistency between DLW and thermodynamic SGR (Park et al., 2015). That is the reason why we exclude the grids with less than 90% sea ice concentration or less than 0.1-meter sea ice thickness. Fig. S12 and S13 show that by such an approach, most regions on the Atlantic side that potentially have a distinct decrease in sea ice concentration have been trimmed out. The remaining sea ice concentration change in the Arctic Ocean is mostly less than 1%.

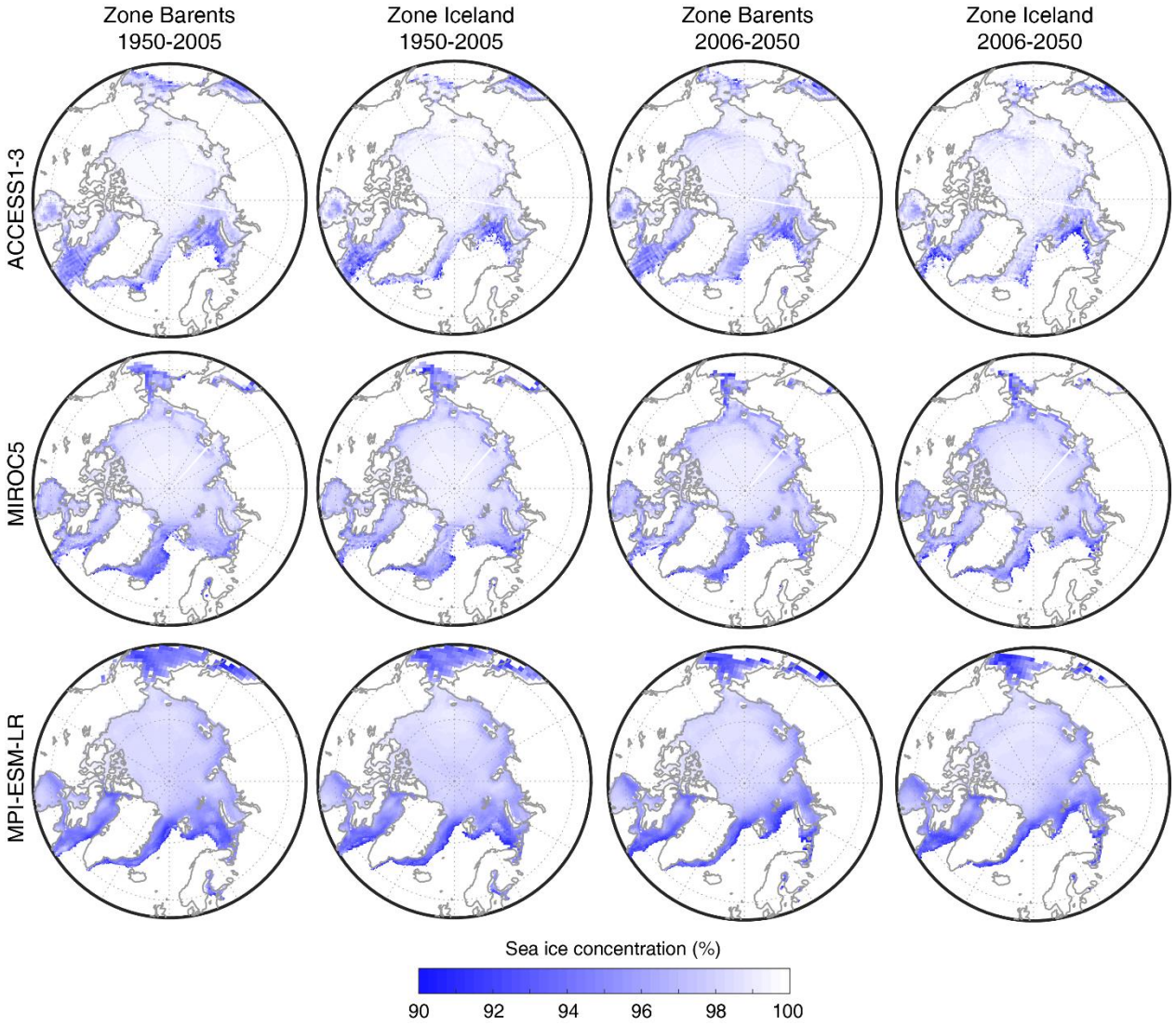

Fig. S14. The composite of sea ice concentration one day before the days of strong cyclones. The patterns only involve sea ice data points with > 90% sea ice concentration and >0.1 m sea ice thickness.

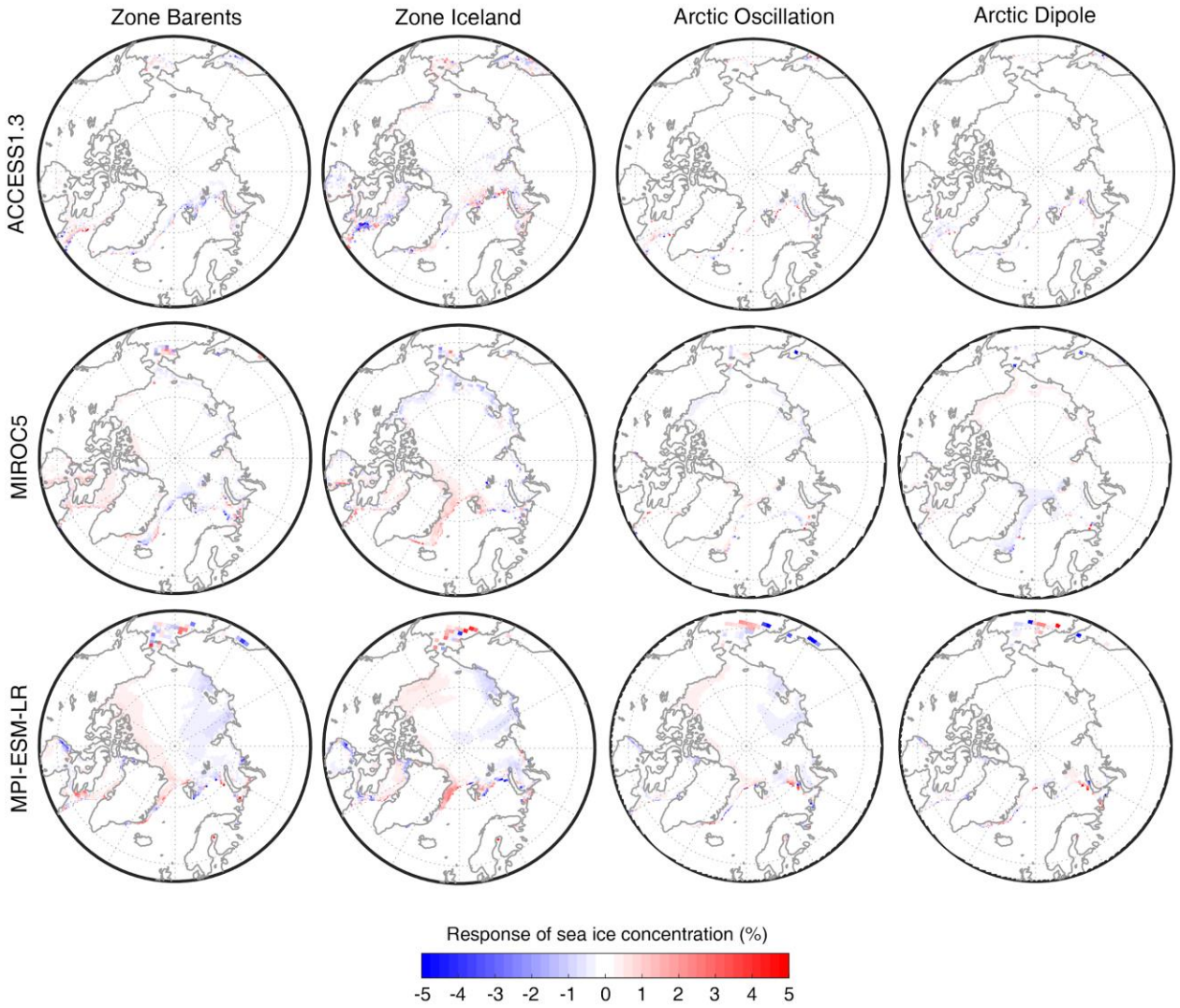

Fig. S15. Anomalies of sea ice concentration in response to strong cyclones and regressed on the large-scale circulations patterns of the positive AO and negative AD in the historical period (1950-2005).

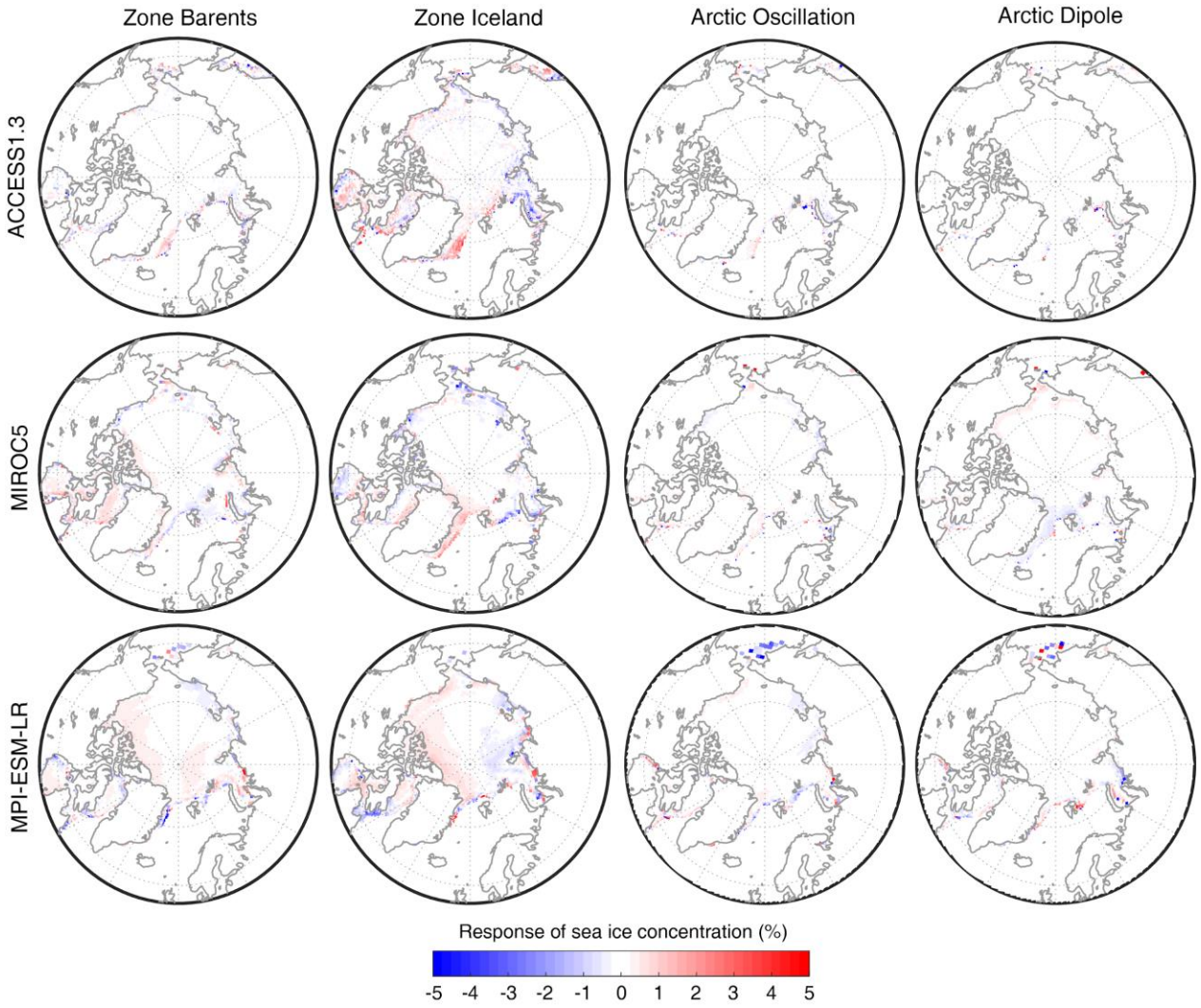

Fig. S16. As for Fig. S12 but in the RCP8.5 period (2006-2050).

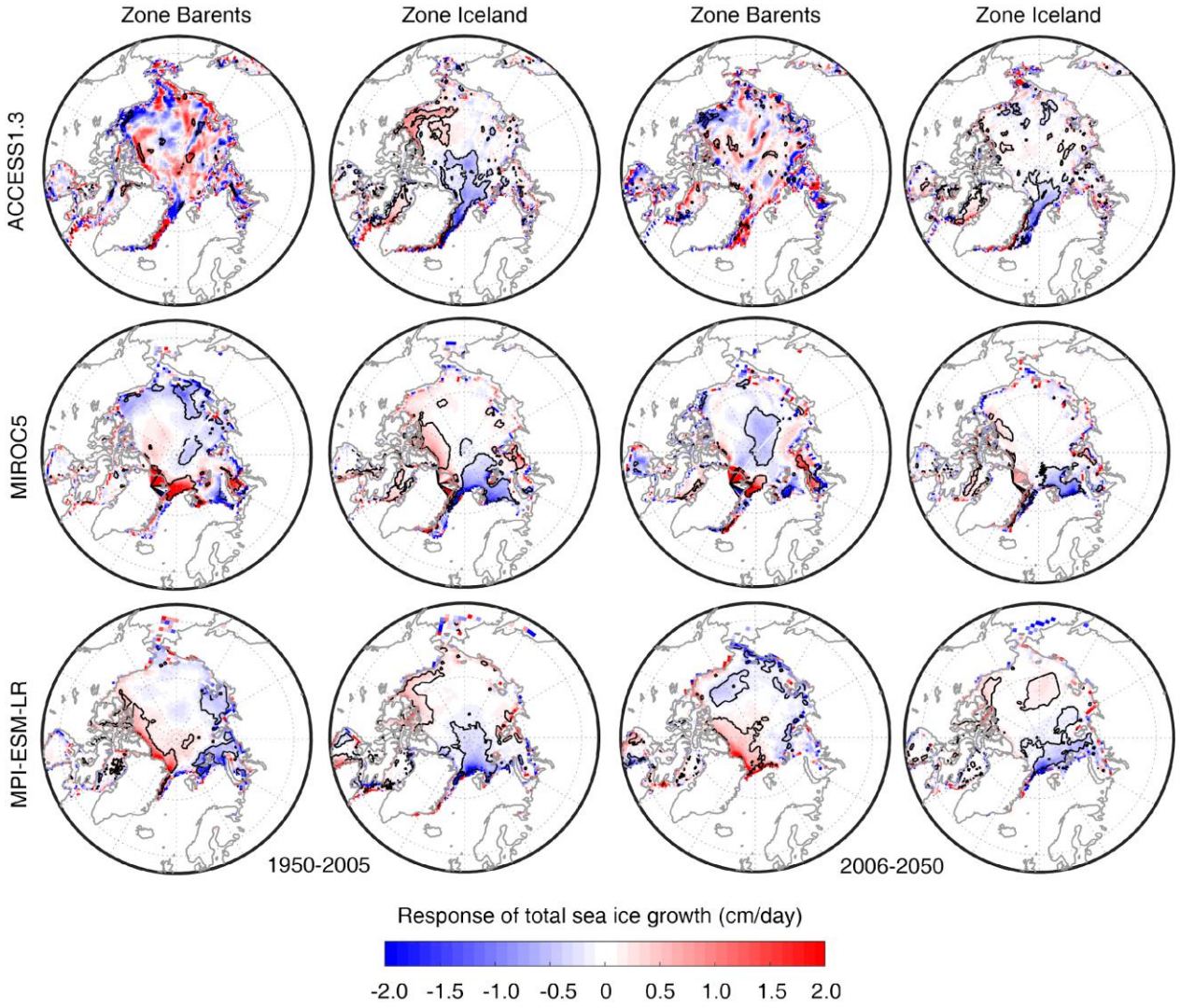

Fig. S17. Anomalies of total SGR (cm/day; shaded) in response to the strong cyclones in Zone Barents and Zone Iceland in the historical period (1950-2005) and projected period (2006-2050). Black solid lines delimit the regions in which the anomaly passes the t-test with a 95% significance level.

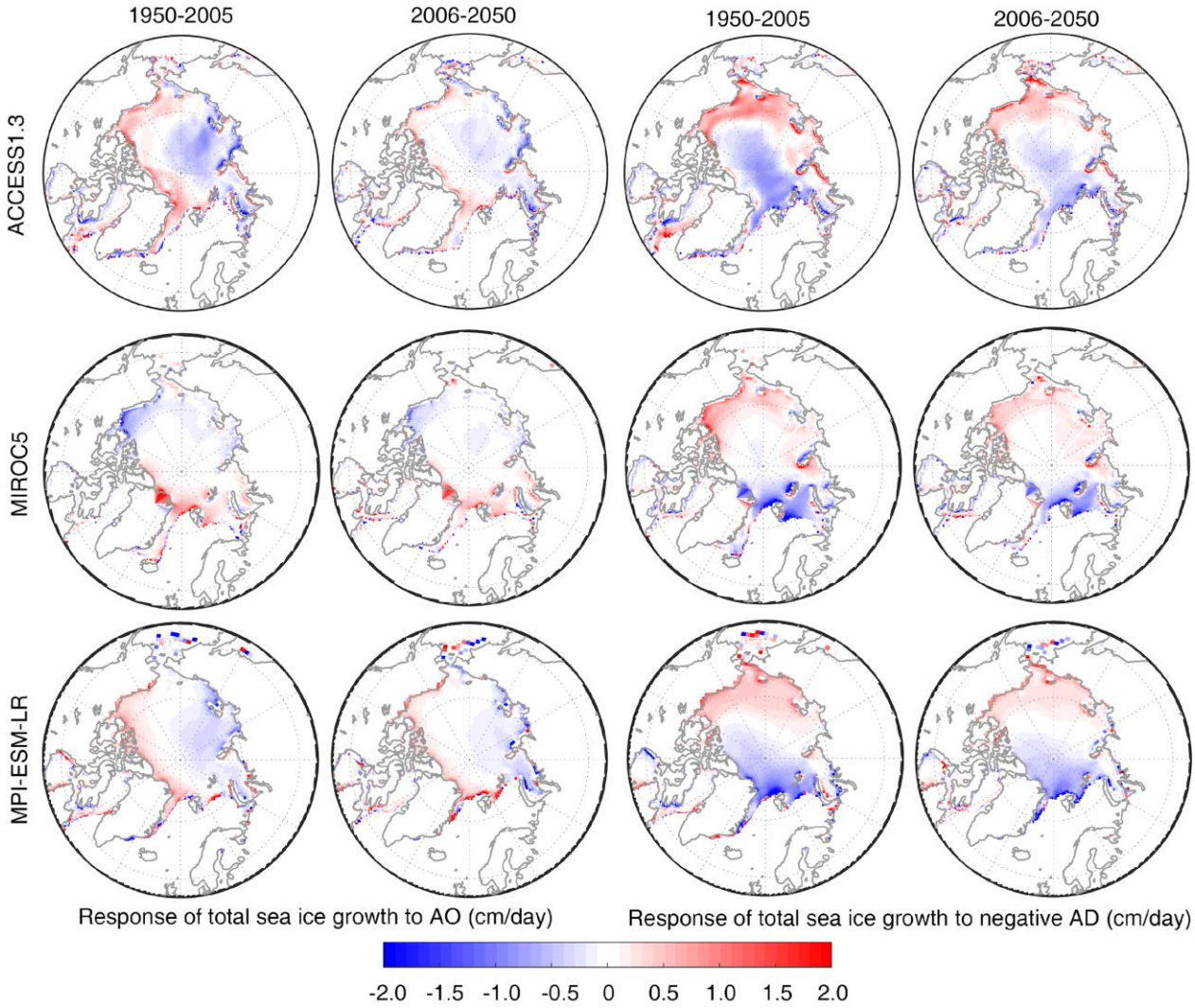

Fig. S18. anomalies of total SGR (cm/day; shaded) regressed on positive AO (left panel) and negative AD (right panel) in the historical period (1950-2005) and projected period (2006-2050).

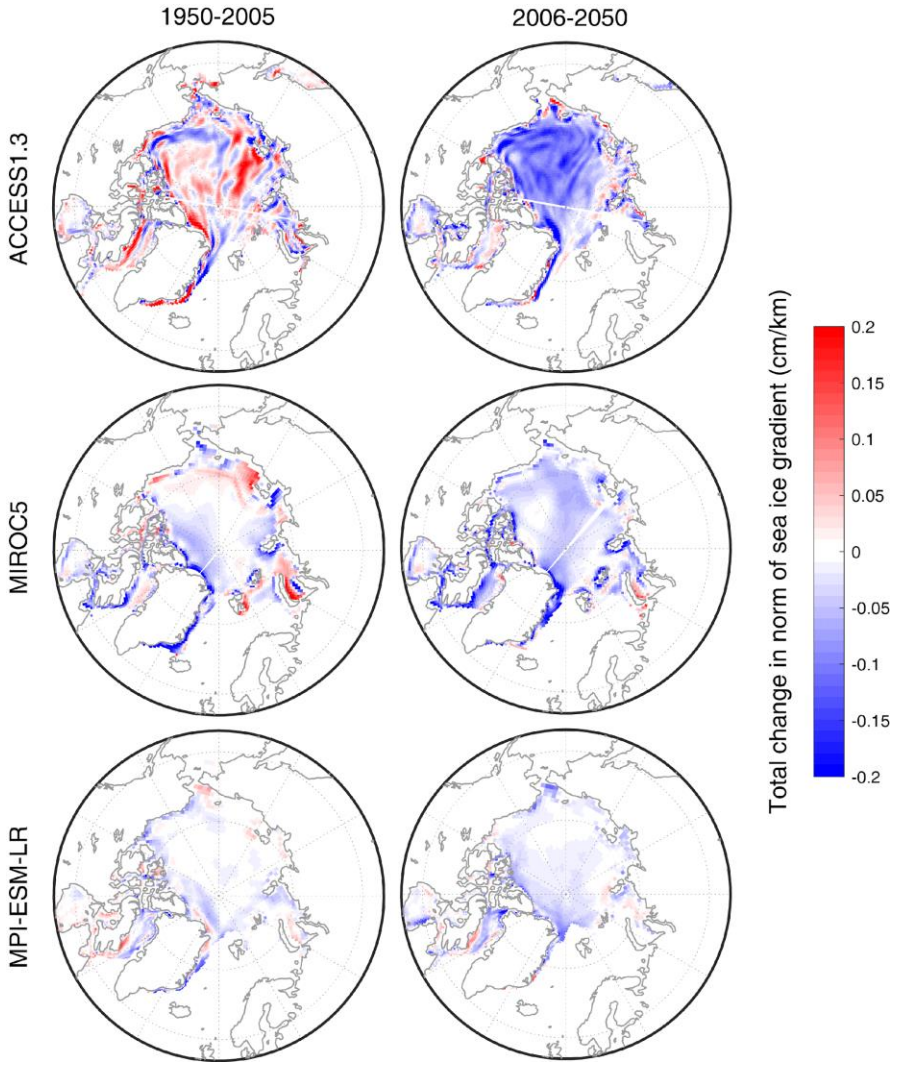

Fig. S19. Total change in the norm of end-of-March sea ice thickness gradient (cm/km; the norm of sea ice thickness gradient is calculated as $\sqrt{(\frac{\partial h}{\partial x})^2 + (\frac{\partial h}{\partial y})^2}$, as the quantification of spatial heterogeneity of sea ice thickness) in both periods. For all three models, the spatial heterogeneity of sea ice decreases with time in general, and it decreases more in the projected period (2006-2050) than in the historical period (1950-2005).

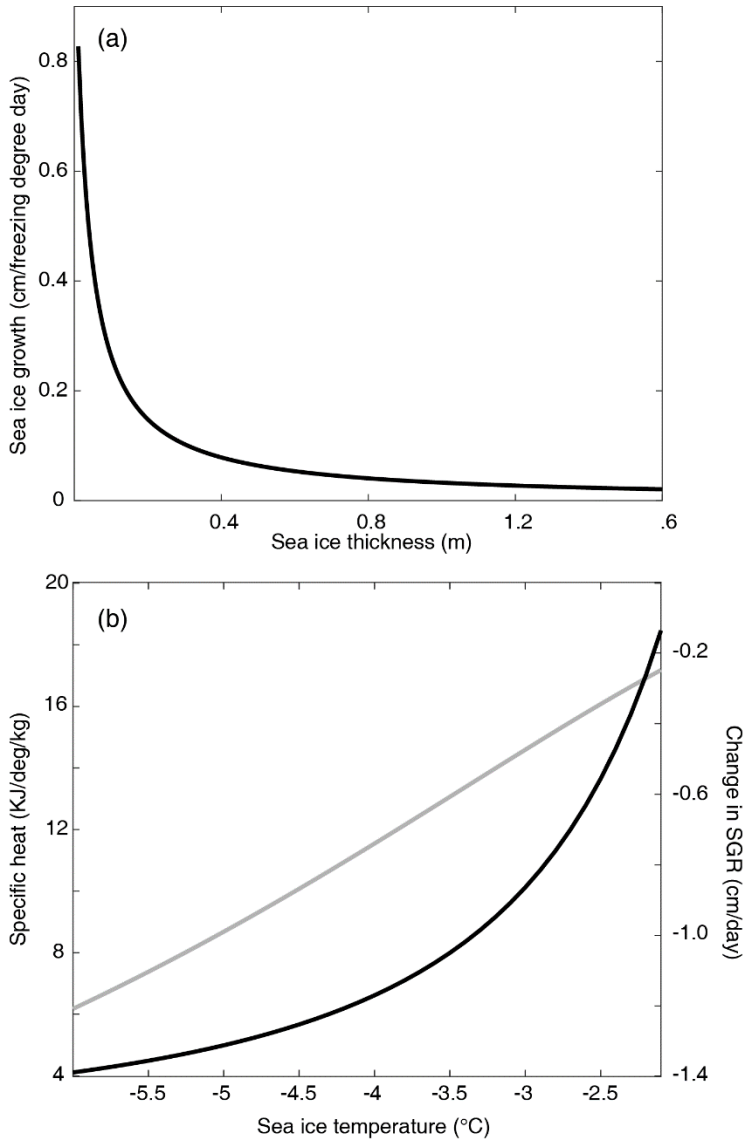

Fig. S20. (a) The empirical sea ice growth rate (cm per freezing degree day) as a function of the base state sea ice thickness from Anderson (1961). (b) The specific heat of sea ice with a maximum salinity as a function of sea ice temperature (black line), and the thermodynamic SGR inhibition per W/m^2 extra longwave radiation added on the last centimeter of old sea ice (assuming a one-centimeter-thick sea ice layer above the newly-grown layer at the bottom) as a function of sea ice temperature. Both curves are derived from the governing equations of thermodynamic sea ice growth/melt in CICE4. The freezing temperature of seawater is set to -2°C to simplify the calculation.

Reference

Cai, L., V. A. Alexeev, J. E. Walsh, and U. S. Bhatt, 2018: Patterns, Impacts, and Future Projections of Summer Variability in the Arctic from CMIP5 Models. *Journal of Climate*, **31,** 9815-9833.

Hunke, E. C., 2010: Thickness sensitivities in the CICE sea ice model. *Ocean Modelling*, **34,** 137-149.

Park, H.-S., S. Lee, S.-W. Son, S. B. Feldstein, and Y. Kosaka, 2015: The Impact of Poleward Moisture and Sensible Heat Flux on Arctic Winter Sea Ice Variability. *Journal of Climate*, **28,** 5030-5040.